Acta Geochim (2025) 44:1377–1394
https://doi.org/10.1007/s11631-025-00824-4

ORIGINAL ARTICLE

C-V fractal modeling of the pyrite thermoelectric coefficient and estimation of continuation of ore bodies at depth in the Pujon gold deposit, DPR Korea

Yon-Ho Kim[1] · Chung-Nam O[1] · Kwang-U Choe[1] · Kwang-Chol Hwang[1]

Received: 12 May 2025 / Revised: 10 July 2025 / Accepted: 3 September 2025 / Published online: 10 October 2025

Abstract This paper describes a method for estimating the continuation of ore bodies at depth based on concentration-volume (C-V) fractal modeling of the pyrite thermoelectric coefficient in the Pujon gold deposit, Democratic People's Republic of Korea. The method is first established using data in the Kumjomdong area, a well-explored brownfield, and it is then applied to estimate the continuation of ore bodies at depth in the Pyongsandok area, a less-explored greenfield. The methodology consists of four steps: (1) 3D modeling of ore bodies using surface geological mapping, mining tunnels in different levels, and a borehole dataset; (2) 3D modeling of thermoelectricity coefficients from Au-bearing pyrites based on discrete smooth interpolation and C-V fractal techniques; (3) determination of levels used for calculation of the thermoelectric parameter of pyrite by C-V fractal modeling instead of traditional levels; and (4) determination of the thermoelectric parameter vertical gradient of pyrite reflecting the variation characteristics of pyrite thermoelectricity in the Pujon deposit. The results indicate that (1) pyrites in the Pujon deposit are dominantly P-type, and it is not reasonable to use traditional levels to calculate the thermoelectric parameter of pyrite; (2) thresholds determined by C-V fractal modeling can be used as levels to calculate the thermoelectric parameter of pyrite; (3) the thermoelectric parameter vertical gradient of pyrite ranges from 1 to 2 in the Pujon deposit; and (4) ore body Pyongsan No. 9 extends 85 m to 235 m downward from the current borehole location.

Keywords Thermoelectricity coefficient of pyrite · DSI · C-V fractal · Pujon gold deposit

✉ Yon-Ho Kim
yh.kim@ryongnamsan.edu.kp

Chung-Nam O
geog3@ryongnamsan.edu.kp

Kwang-U Choe
ku.choi1025@ryongnamsan.edu.kp

Kwang-Chol Hwang
geog2@ryongnamsan.edu.kp

[1] Faculty of Geology, Kim Il Sung University, Pyongyang, Democratic People's Republic of Korea

1 Introduction

Pyrite is one of the most common Au-bearing sulfides in hydrothermal gold deposits, and its typomorphic characteristics such as crystalline behavior, thermoelectricity, and chemical composition are generally controlled by different physicochemical environments during formation (Abraitis et al. 2004; Li et al. 2012, 2020; Shen et al. 2013; Wang et al. 2016, 2022; Alam et al. 2023). Thus, typomorphic characteristics of pyrite can be used not only in studying the genesis of gold deposits, but also for exploration, particularly for deep ore predictions. Typomorphic characteristics of pyrite such as thermoelectricity in different ore bodies or different ore-forming stages can be analyzed in metallogenic studies to support mineral prospecting (Shen et al. 2013; Xue et al. 2014; Wang et al. 2016, 2019, 2021; Geng et al. 2018; Alam et al. 2019; Wu et al. 2021, 2024).

In previous studies of pyrite thermoelectricity, the pyrite thermoelectric parameter (Xnp) is typically calculated based on thermoelectric coefficients using four constant levels with certain intervals, and the values of Xnp are then used to calculate the vertical gradient of Xnp (VH) and estimate the erosional level of gold deposits (γ) as an empirical formula (Xue et al. 2014;

Wang et al. 2016). However, it may be unreasonable to use four constant levels in the empirical formula even in cases of either dominant P-type or dominant N-type pyrites, because the range of values is quite different from the typical cases. Different gold deposits may have their own levels of thermoelectric coefficients of pyrite in the samples used to calculate the pyrite thermoelectric parameter.

Most previous investigations (Wang et al. 2016, 2021; Geng et al. 2018; Alam et al. 2019; Wu et al. 2021, 2024) have focused on case studies using well-established methods in this field, and studies on the development of more sophisticated methods using measured thermoelectric coefficient data have not been reported. Thus, studies are needed to develop improved methods using thermoelectric coefficient data for pyrite to calculate parameters representing the continuation of ore bodies at depth, ensuring that the results are highly consistent with the measured data in the study area.

In the Pujon deposit, the Kumjomdong, West Kumjomdong, and Wondong areas around the Kumjomdong fault are relatively well explored, and the continuation of ore bodies at depth has largely been clarified. Meanwhile, the Pyongsandok area around the Kurumryong fault has been less explored and is considered to be a promising area in the Pujon deposit. Thus, the identification of more gold reserves at depth is critical for the development of the Pujon gold mine. The present study mainly focuses on the thermoelectric characteristics of gold-bearing pyrite and its application to deep ore estimation in the Pujon deposit.

In this paper, we address the question of how we can estimate the continuation of ore bodies at depth using pyrite thermoelectricity in the Pujon gold deposit, where pyrites are dominantly P-type. The main aims of the paper are (1) to establish the method to calculate the thermoelectric parameter of pyrite using thresholds determined by C-V fractal modeling, (2) to determine the appropriate thermoelectric parameter vertical gradient of pyrite in the Pujon deposit, and (3) to estimate the continuation of the ore body Pyongsan No. 9 at depth.

In the geosciences, fractal models have been used to explain the spatial distributions of geological features, and several fractal models have been developed and successfully adopted to study spatial features related to mineralization, such as geological controls (Bazargani et al. 2025) and geochemical anomalies (Pourgholam et al. 2021; Sadeghi 2021; Hosseini et al. 2022; Yilmaz et al. 2022; Pourgholam et al. 2024). Considering the previous literature and recent studies, geological features such as geochemical anomalies and fault distribution have fractal dimensions. In the current study, we used a data-driven C-V fractal model for discretization of spatially continuous values of pyrite thermoelectricity in order to obtain discretized levels used for calculation of the thermoelectric parameter of pyrite.

1.1 Geological setting

The Pujon deposit is situated in Chail district of Pujon county, South Hamgyong Province, Democratic People's Republic (DPR) of Korea. The study area is tectonically located on the eastern part of the Pujongang fault zone, Rangnim Massif, Sino-Korean Craton (Fig. 1). The Pujon deposit borders the Hyesan-Riwon Basin on the east, and it is located near the contact between the Rangnim Massif and Hyesan-Riwon Basin. This region is considered to be one of the most abundant areas of polymetallic mineralization in DPR Korea because of the complexity and superposition of geological structures and diversity of magmatism (Paek et al. 1993). This area was selected for three practical reasons: (1) it is necessary to answer the question of whether ore bodies are continuous at depth, (2) pyrite is a principal mineral occurring in the study area, and (3) geological datasets such as borehole data are readily available. The study area can be divided into the Kumjomdong, West Kumjomdong, Wondong, and Pyonsandok districts.

The geology of the study area essentially consists of granite gneiss (Neoarchean Rangnim Group) and granitic intrusions (Neoarchean Ryonhwasan Complex) (Fig. 2). In addition, some dykes of the Jurassic Tanchon Complex are intruded into the NE-trending fissures. The rocks of the Rangnim Group are small and irregularly shaped. NS-, EW-, NE-, and NW-trending fault systems are developed in this area. The NS-trending fault system is 1 km wide and 200 km long and consists of the Pujongang fault zone and

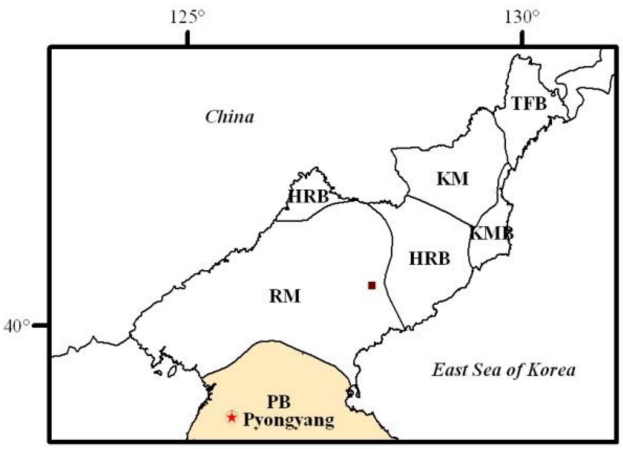

Fig. 1 Location of the study area (the red box indicates the location of the study area). TFB, Tumangang Fold Belt; KM, Kwanmo Massif; KMB, Kilju-Myongchon Basin; HRB, Hyesan-Riwon Basin; RM, Rangnim Massif; PB, Phyongnam Basin (Paek et al. 1993)

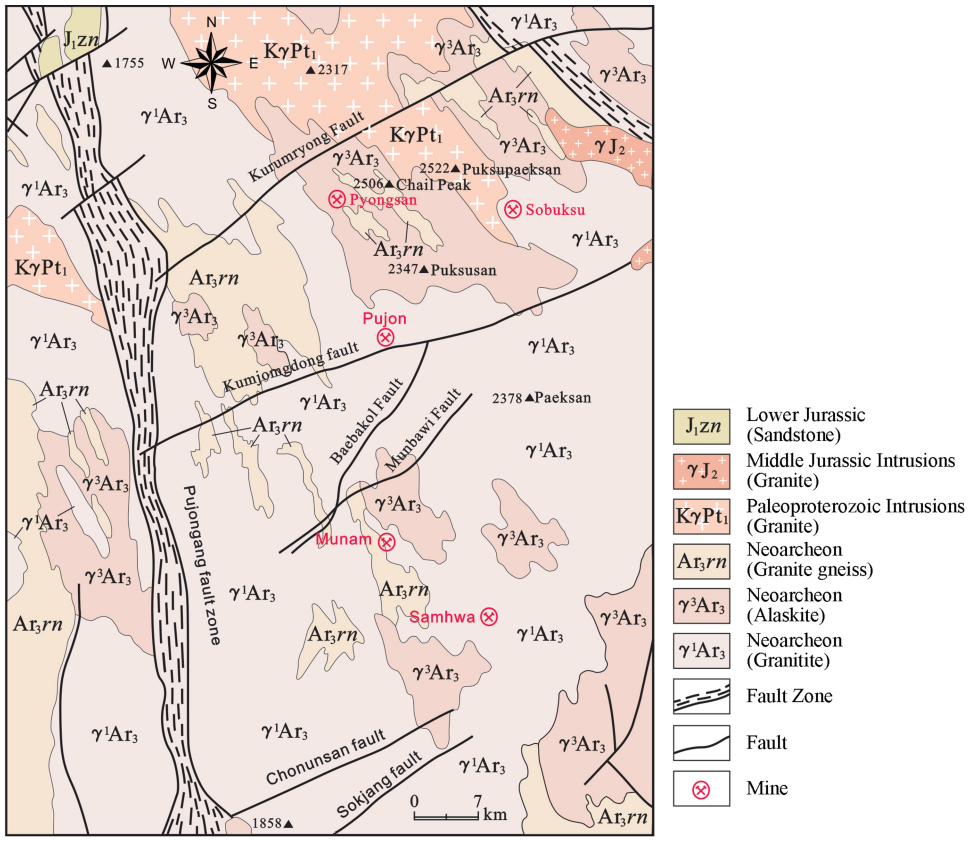

Fig. 2 Geological map of the study area

some faults parallel to it. This fault system acts as a pathway in the mineralization. The EW-trending fault system was formed just before the NE-trending fault system, and it acts as a pathway and partly as traps in the mineralization. The NE-trending fault system with length varying from hundreds of meters to 2000 m and width of 10 m played the most important role in the mineralization. It involves Kumjomdong, Tohwadong and 6.15 faults. They are mainly NEE-trending, with dips of 50° to 70° to the NNW. The NW-trending fault system with width varying from 10 to 20 m and length of 400–1000 m is not essentially related to the mineralization. The formation sequence of different fault systems in this area is NS-, EW-, NE-, and NW-trending. The rocks in the NE-trending fault system were highly fractured by other fault systems, and ore-bearing quartz veins were intruded into the fissures to form the mineralization.

1.2 Deposit features

The gold deposit contains more than 20 gold-bearing veins, which are divided into two groups: an auriferous quartz type involved in the fault fissures, and a silicification type occurring at the top and bottom of the fault fissures (Choe et al. 2011). Silicification is the main type, and all but veins Nos. 2 and 3 occur in the silicification zones. Vein No. 1 was formed by the penetration of a quartz vein and sulfide veinlets into fractured breccia zones within parent rocks filling in the ore-bearing structures with a strike of 75° to 80°. Vein No. 6 was formed by the penetration of auriferous quartz veins and sulfide veinlets into fissures along the footwalls of ore-transporting structures and micro-fissures in the parent rocks. This is a large deposit, and the Au grade is high. The shapes of ore bodies differ slightly from place to place. There are many lenticular quartz veins in the west, and irregular silicification types are rich in the east. The veins generally occur as an echelon in the plane maps.

The length of ore bodies in the direction of the strike is about 4 km, and the veins are continuous with a range of 2.3 km. The maximum width is 31.5 m in the silicification zones and 10.5 m in the quartz veins. Ore bodies consist of quartz and a small amount of sulfides. The quartz occurs with two colors—white and gray—and the gay quartz is rich in the lower level of ore bodies. Sulfides are involved in ore bodies with an average of 5%. The auriferous quartz veins are lenticular with a short length and thick width of 0.5 m on average. The thickness of ore bodies in K-feldspathization and silicification zones varies from 5 to 20 m, with an average of 7 m, and they continue for a length of 300–400 m in the direction of the strike. Vein No. 6 in the Kumjomdong district occurs in ore bodies of auriferous sulfides + quartz + silicification. The ore-bearing and Au-bearing ratios are 22.5% and 61.7%, respectively. The maximum Au grade is

24.29 g/t and the ratio of natural gold is 30%–40%. The Au grade of the deposit is 4–10 g/t, with an average of 6.67 g/t. The ore minerals are quite different in the deposit. The metal ore minerals include pyrite, chalcopyrite, native gold, native silver, galena, sphalerite, hematite, magnetite, molybdenite, and siderite. The nonmetal ore minerals are quartz, K-feldspar, chlorite, epidote, muscovite, and sericite. The secondary minerals include limonite, chalcocite, covellite, azurite, bornite, calcite, and ankerite. Natural gold is involved in almost all the minerals such as white and gray quartz, pyrite, chalcopyrite, and galena, but the content is different from minerals. The maximum Au grade is 100 g/t in chalcopyrite, 150 g/t in galena, and tens of grams per tonne in pyrite. The size of Au particles varies from 0.01 to 0.8 mm, with 60%–70% in the range of 0.06–0.2 mm. Most of the Au crystals (more than 70%) have dendritic and ameboid shapes. The Au/Ag ratio is relatively low compared with other gold deposits in our country. The gold is closely related to the copper, and the Au grade is proportional to the Cu grade in the direction of the strike. The main sulfides are chalcopyrite and pyrite. In addition, metal minerals including galena, sphalerite, hematite, and limonite are present. Galena is rich in the lower level of the deposit. Pyrite is the primary Au-bearing mineral in the Pujon deposit. With regard to gold, fracture-filled boundary gold occurs more often than inclusion gold. In the current study, pyrite is considered to be an indicator for estimating the continuation of ore bodies at depth in the Pujon deposit.

Pyrite occurs in almost all the Au ore bodies, and it is rich in massive rocks with small gold and silver crystals. Pyrite does not include As, and it is rich in nickel and copper. The mineralization in the deposit is characterized by K-feldspar, auriferous sulfide, a barren quartz vein, and calcite. Au mineralization was formed in the stage of auriferous sulfide. The parent rocks around the ore bodies are characterized by K-feldsparthization, chloritization, and sericitization. The genesis of the deposit is considered to be hypothermal and mesothermal.

2 Methods

The methodology used in the current study includes the measurements of the thermoelectric properties of pyrite using a thermoelectric coefficient measuring instrument, discrete smooth interpolation (DSI) modeling of thermoelectric data, and concentration-volume (C-V) modeling. DSI was implemented in GOCAD software and C-V modeling in MATLAB software.

2.1 Thermoelectricity of pyrites

2.1.1 Thermoelectric theory

Pyrite is a typical semiconductor mineral, and under different temperature conditions, it generates a thermal electric force known as the Seebeck effect. The thermoelectric phenomenon is strongly dependent on the chemical composition of pyrites, and the thermoelectric coefficient of pyrite can be calculated as follows (Shao et al. 1990):

$$\alpha = \frac{\pm E}{t_H - t_C}\left(\pm\frac{\mu V}{^\circ C}\right), \tag{1}$$

where t_H and t_C are the hot-end and cold-end temperature, respectively. The positive and negative sign of E is correlated with the positive and negative properties of the carriers with a certain conduction type, and the conduction type can be either N-type or P-type. The values of α and the conduction type of pyrite are influenced by isomorphous impurities in the composition of pyrite, defects in crystal structure, density, and external excitation conditions (e.g., temperature and pressure gradients). The pyrite thermoelectricity can be used as an indicator of the depth of the ore-forming processes, because these factors are influenced by conditions at the depth of ore formation (Abraitis et al. 2004; Zhang et al. 2010; Shen et al. 2013; Wang et al. 2016).

2.1.2 Measurement of thermoelectric properties of pyrite

The thermoelectric properties of the pyrite samples were measured using the THERMO-24 thermoelectric coefficient measuring instrument at the Ore Deposits Laboratory, Kim II Sung University. The temperatures of the cold end and hot end were set to 20°C and 80°C, respectively. Twenty grains of pyrites per sample were selected for measurement, and each grain was larger than 0.2 mm. The measurement data are summarized in Table 1. The thermoelectricity measurements were obtained from 1957 grains of pyrites from a total of 45 samples from 11 ore bodies of 27 different levels of the Pujon deposit. The data indicate that N- and P-type pyrites comprise on average 1.4% and 98.6%, respectively.

Therefore, most of the pyrites in the Pujon deposit are P-type, and N-type pyrites are measured only in some ore bodies of Wondong and West Kumjomdong and in ore body No. 12 of Kumjomdong. The statistics regarding P-type thermoelectricity are summarized in Table 2.

Table 1 Measured thermoelectric data of pyrites from the Pujon deposit

Ore body	Level (m)	N-type thermoelectricity,$\alpha(\mu V \cdot {}^{\circ}C^{-1})$			N (%)	P-type thermoelectricity,$\alpha(\mu V \cdot {}^{\circ}C^{-1})$			P (%)
		Maximum	Minimum	Average		Maximum	Minimum	Average	
Wondong No.1	1441	–	–	–	–	215.9	98.5	136.9	100
Wondong No.5	1392	−25.8	−170.4	−115.9	6.3	207.8	52.8	125.4	93.7
Wondong No.5	1336	−26.4	−221.5	−85.9	46.1	215.5	46.7	148.3	53.9
West Kumjomdong No.1	1390	–	–	–	–	240.8	77.9	148.8	100
West Kumjomdong No.1	1352	−85.4	−197.2	−160.9	9	197.8	74.3	121.7	91
Kumjomdong No. 6	1775	–	–	–	–	181.2	87.9	122.8	100
Kumjomdong No. 6	1748	–	–	–	–	201.4	107.8	141.6	100
Kumjomdong No. 6	1722	–	–	–	–	136.1	81.5	108.4	100
Kumjomdong No. 6	1694	–	–	–	–	303.7	97.6	164.2	100
Kumjomdong No. 6	1682	–	–	–	–	278.0	106.0	167.7	100
Kumjomdong No. 6	1628	–	–	–	–	132.9	67.2	109.7	100
Kumjomdong No. 1	1583	–	–	–	–	146.6	109.7	129.5	100
Kumjomdong No. 2	1635	–	–	–	–	216.8	125.8	159.5	100
Kumjomdong No. 2	1591	–	–	–	–	162.2	91.0	127.2	100
Kumjomdong No. 14	1913	–	–	–	–	231.5	119.8	159.5	100
Kumjomdong No. 14	1902	–	–	–	–	453.7	163.8	232.2	100
Kumjomdong No. 14	1900	–	–	–	–	139.6	96.5	118.7	100
Kumjomdong No. 14	1877	–	–	–	–	148.1	98.5	120.5	100
Kumjomdong No. 14	1863	–	–	–	–	186.2	90.7	128.5	100
Kumjomdong No. 14	1856	–	–	–	–	195.6	99.2	139.20	100
Kumjomdong No. 14	1801	–	–	–	–	157.2	98.7	127.2	100
Kumjomdong No. 14	1775	–	–	–	–	178.8	81.4	127.2	100
Kumjomdong No. 15	1856	–	–	–	–	180.9	68.7	114.4	100
Kumjomdong No. 12	1941	–	–	–	–	169.0	76.1	120.7	100
Kumjomdong No. 12	1902	–	–	–	–	182.9	69.9	112.6	100
Kumjomdong No. 12	1888	–	–	–	–	219.2	73.1	144.4	100
Kumjomdong No. 12	1881	−56.9	−287.2	−175.4	68.6	184.8	53.3	131.4	31.4
Kumjomdong No. 12	1873	–	–	–	–	165.6	81.3	130.0	100
Kumjomdong No. 11	1815	–	–	–	–	217.2	111.3	154.9	100
Kumjomdong No. 7	1710	–	–	–	–	161.8	88.8	123.4	100

Table 2 Statistics of P-type pyrite thermoelectricity

Number of samples	Minimum	Median	Maximum	Mean	Std	Variance
43	21.04	127.41	232.19	132.02	32.13	1032.54

2.1.3 Variations in pyrite thermoelectric coefficients in the Pujon gold deposit

The regression line for the average thermoelectric coefficients of the pyrite in levels can be plotted as shown in Fig. 3. The regression line indicates that the average thermoelectric coefficients of the pyrite in the Pujon deposit increase at depth. This is consistent with the thermoelectric theory, and the thermoelectric coefficients of the pyrite can be used to estimate the continuation of ore bodies at depth.

The thermoelectric parameter of the pyrite (Xnp) can be calculated based on the thermoelectric coefficient (Yang and Zhang 1991; Shen et al. 2013; Xue et al. 2014; Wang et al. 2016):

$$Xnp = \left(2f_{\mathrm{I}} + f_{\mathrm{II}}\right) - \left(f_{\mathrm{IV}} + 2f_{\mathrm{V}}\right), \tag{2}$$

where f corresponds to the levels of thermoelectric coefficients of pyrites in the samples as follows: f_{I} represents $\alpha > 400$ μV/°C, f_{II} represents α in the range of 200–400 μV/°C, f_{III} represents α in the range 0–200 μV/°C, f_{IV} represents α in the range of 0 to −200 μV/°C, and f_{V} represents $\alpha < -200$ μV/°C. It is inappropriate to calculate the values of Xnp of pyrites in the Pujon gold deposit using

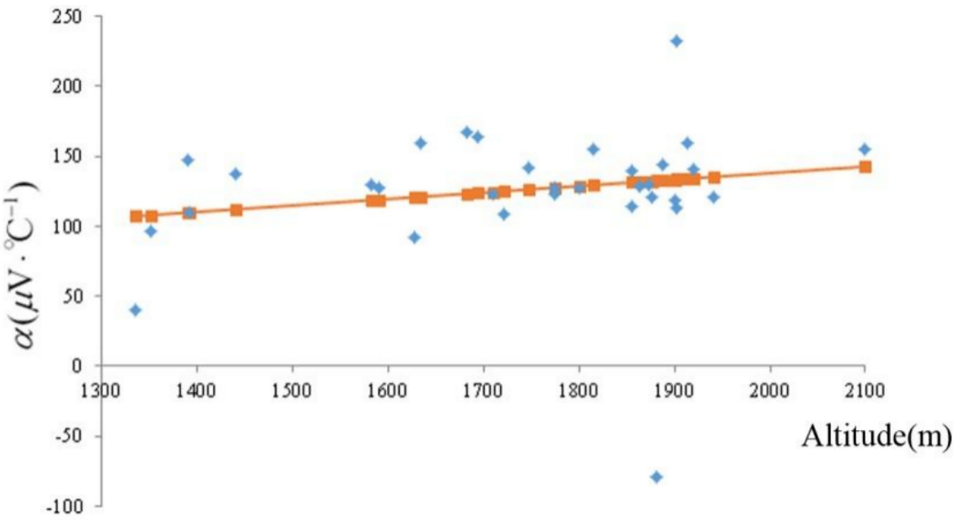

Fig. 3 The regression line for the average thermoelectric coefficients of the pyrite in levels

the same *f* levels as in Eq. (2), because most of the measured thermoelectric data are P-type, and levels of thermoelectric coefficients of pyrites can be different from deposits. In the case of the Pujon gold deposit, the lower boundaries of almost all ore bodies have been approximately determined by drilling. It is necessary to determine alternative levels of thermoelectric coefficients of pyrites in the samples corresponding to the Pujon gold deposit instead of traditional levels used in Eq. (2). In the current study, new levels of thermoelectric coefficients of pyrites to calculate the thermoelectric parameter of pyrite were determined by C-V fractal modeling.

2.2 C-V fractal modeling

2.2.1 Building datasets

The datasets available for 3D modeling in the Pujon deposit area include 1:2000 scale geologic data, a digital elevation model (DEM), an exploratory engineering layout plan per level at 100 m, 50 m, 0 m, −45 m, −90 m, −145 m, −185 m, and −225 m, and related prospecting line profile maps. These datasets were used to model the ore bodies and geology in the Pujon deposit area in 3D. The X coordinates of the model area range from 270,646 to 276,943 m, the Y coordinates from 1,951,780 to 1,954,370 m, and the Z coordinates from 930 to 2140 m. The model area at the surface measures 16.32 km^2, and the

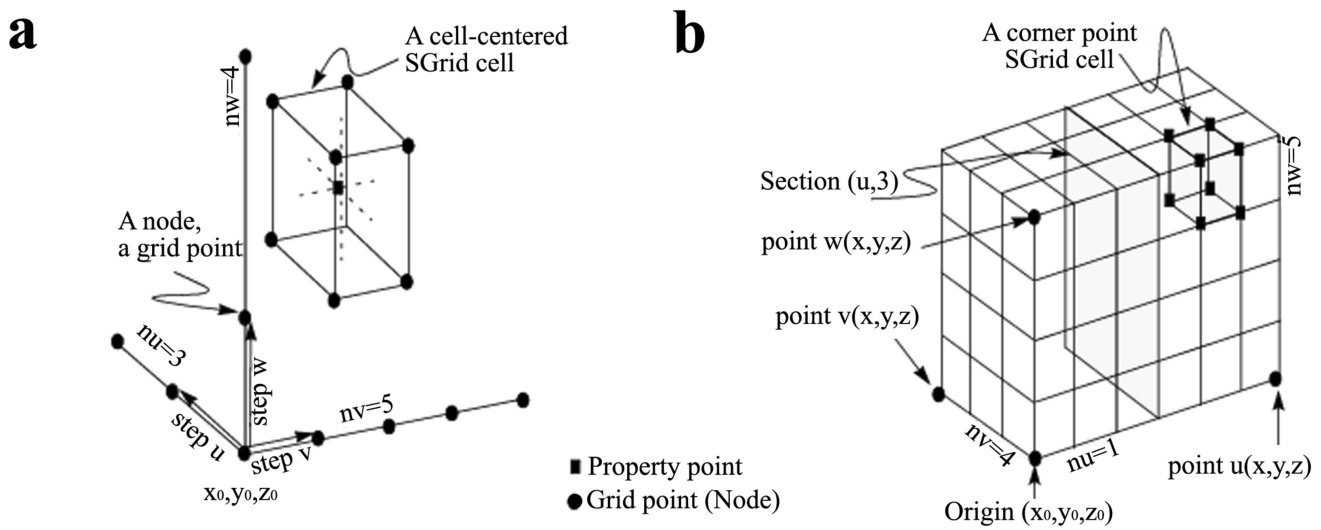

Fig. 4 Graphical examples of an SGrid object and its components: **a** SGrid and its step-vectors, and **b** SGrid and its end-points (Micromine 2015)

total volume of the Sgrid is 6300×2590×1210 m^3 (Fig. 4). The 3D ore body model region contains ore bodies Nos. 1, 2, 10, 12, and 13, which represents 12% of the volume of the 3D block model of the study area.

Thermoelectric coefficient data from the Pujon deposit are discrete and sparse, and therefore it is impossible to use geostatistical techniques because we cannot calculate the semivariograms in the horizontal and vertical directions in 3D space. Therefore, the discrete smooth interpolation (DSI) technique in GOCAD was applied to build 3D geological and thermoelectricity models.

2.2.2 DSI method and SGrid

Geological processes such as mineralization occur in 3D, and they are better represented by their geological signatures in 3D datasets. Thus, geological modeling is best modeled in 3D versus 2D space. However, regional-scale 3D geological modeling is rarely feasible, mainly because regional-scale public-domain 3D datasets over large areas are generally not available (Xiao et al. 2015). On the other hand, deposit-scale 3D datasets for specific areas are occasionally available, and can be used for delineating further drilling targets at the deposit scale. In addition, commercial 3D GIS products such as GOCAD, Surpac, and Micromine (Geovia 2015; Micromine 2015; Wang et al. 2020) have become widely available, and this has led to the development of 3D geological models, particularly at detailed scales (Xiao et al. 2015; Mohammadpour et al. 2021; Deng et al. 2022). One of the main challenges in 3D geological modeling based on 3D GIS is to efficiently incorporate 3D predictive models within 3D GIS, because most commercial 3D GIS software does not include corresponding models, modules, and tools for 3D geological modeling (Li et al. 2016).

GOCAD is a software program which uses DSI as the core interpolation algorithm (Mallet 2002). It can be used to build a surface or subsurface element with a triangular grid structure, and can be reconstructed using ArcGIS and other GIS software (Perrouty and Lindsay 2014). The basic element of the DSI method is the establishment of a connected network among discretization points in 3D space. If the values of network points meet the constraint criteria, the values at unsampled points can be obtained by computing linear equations (Mallet 2002). DSI is particularly suitable for 3D implicit spatial modeling of natural objects combining explicit spatial distribution of geological properties and usually sampled at a few discrete locations such as drill holes.

In this study, we use SGrid in GOCAD 2015 software to build a 3D geological model according to the need for 3D modeling after building datasets in the ArcGIS 10.4 platform. An SGrid object is a flexible, 3D grid for modeling properties, computing reservoir volumes, and creating flow simulations in GOCAD. An SGrid object can contain property values either at the center or the corners of its cells. The dimensions of the SGrid are defined by its origin, the three axes, the number of points along each axis, and the three step vectors of each cell (Fig. 4). This object is important in reservoir geology and engineering, where anisotropy plays a significant role in hydrocarbon migration and accumulation. In this case, we use SGrid as the main object for 3D modeling of the thermoelectric coefficient of pyrites.

2.2.3 C-V fractal modeling theory for threshold calculation

The C-V fractal model in 3D space proposed by Afzal et al. (2011) was based on the concentration-area fractal model proposed by Cheng et al. (1994) and used by other researchers (Yousefi et al. 2015; Chen et al. 2018; Sadeghi 2021; Yilmaz et al. 2022; Hosseini et al. 2023) to separate geochemical anomalies from background in 2D space. Various researchers demonstrated that the C-V fractal model in 3D space could be used for distinguishing and identifying the mineralizations in their study areas (Afzal et al. 2011; Wang et al. 2013; Zuo et al. 2015; Karaman et al. 2021; Zhang et al. 2021; Paravarzar et al. 2023; Ullah et al. 2023; Heidari et al. 2024). The C-V fractal model can be expressed as follows (Afzal et al. 2011):

$$V(\rho \le \nu) \infty \rho^{-a_1}; V(\rho \ge \nu) \infty \rho^{-a_2}, \tag{3}$$

where $V(\rho \le \nu)$ and $V(\rho \ge \nu)$ denote two volumes with concentration values (ρ) less than or equal to and greater than or equal to, respectively, the value (ν), which represents that threshold of a zone (volume); and a_1 and a_2 are fractal dimensions.

The C-V fractal method has also been used to calculate thresholds and delineate mineralized zones, and the thresholds calculated from the C-V fractal model are useful for mapping the boundaries between different ore zones (Afzal et al. 2013; Wang et al. 2013; Li et al. 2016). In the current study, the C-V fractal model was implemented to calculate thresholds of the thermoelectricity data of pyrites.

2.2.4 Modeling the distribution of the thermoelectric coefficients of pyrite in 3D

The P-type thermoelectric coefficients of pyrite were interpolated using DSI based on a 3D grid cell size of $31 \times 35 \times 24$ m^3. The total number of Sgrid cells is

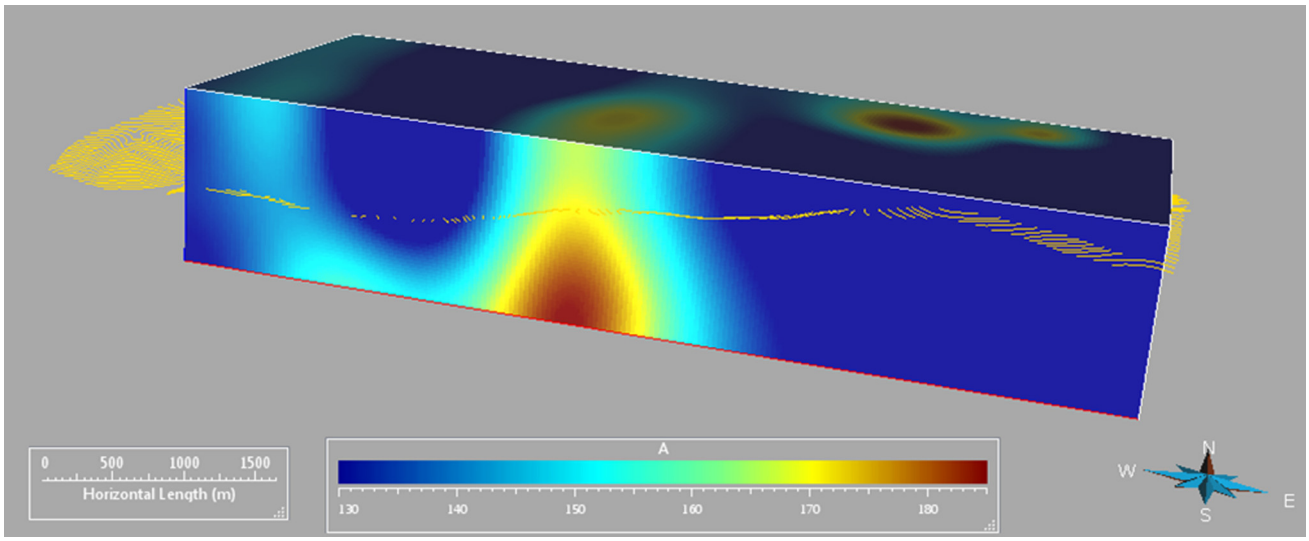

Fig. 5 Sgrid of thermoelectric coefficient by DSI

Table 3 The X, Y coordinates and thermoelectric coefficient thresholds of pyrite calculated by C-V fractal modeling

No.	X	Y	Thermoelectric coefficient thresholds
1	3.82	13.82	45.49
2	4.39	13.82	80.99
3	4.77	13.80	117.53
4	4.93	12.38	138.38
5	5.22	6.22	184.68

Table 4 The coefficients of fitting lines ($Y = mx + b$) in the C-V fractal model

No.	m	b	Goodness of fit (R)
1	−0.00002	13.82	0.92
2	−0.00029	13.82	0.99
3	−0.03	13.95	0.96
4	−8.69	55.25	0.94
5	−21.34	117.59	0.92
6	−11.54	66.46	0.95

$200 \times 80 \times 50 = 800{,}000$. We constructed the 3D model of pyrite thermoelectric coefficients using DSI (Fig. 5).

C-V thresholds and their classification numbers were calculated in the MATLAB R2015a platform (Tables 3 and 4). The goodness of fit is based on the correlation coefficient R. The standard for the goodness of fit in C-V fractal modeling was set to $R = 0.9$ (Fig. 6).

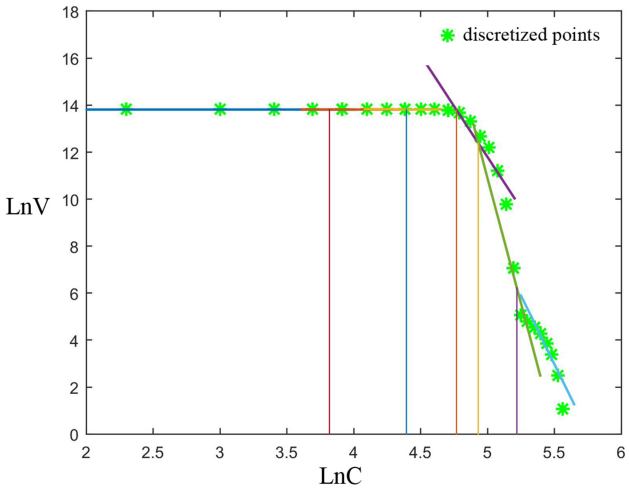

Fig. 6 C-V fractal model of pyrite thermoelectric coefficients

The SGrid cells within the range of 138.38–184.48 $\mu V \cdot {}^{\circ}C^{-1}$ P-type thermoelectric coefficients are consistent with the 3D modeling results of ore bodies from the geological database (Fig. 7).

The Au grade DSI was applied to validate the results of C-V fractal modeling (Fig. 7). The distribution of Au grade did not obey normal distribution and it was impossible to directly use the geostatistical techniques such as kriging. Some additional steps including logarithmic transformation would be needed and variogram function should be subjectively fitted. To reduce the subjectivity in the interpolation, we used DSI instead of geostatistical techniques. As shown in Fig. 8, the Au grade of ore body No. 12 by DSI increases at depth, although it is smaller than the grade in the upper levels. This suggests good

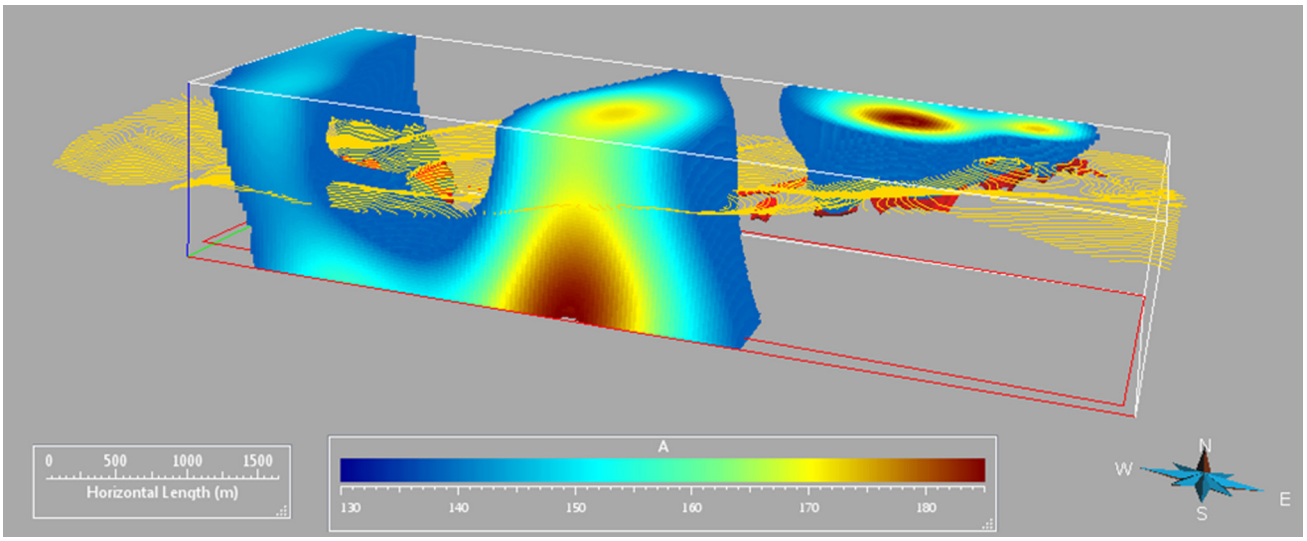

Fig. 7 SGrid cells within the range of 138.38–184.48 $\mu V \cdot {}^{\circ}C^{-1}$

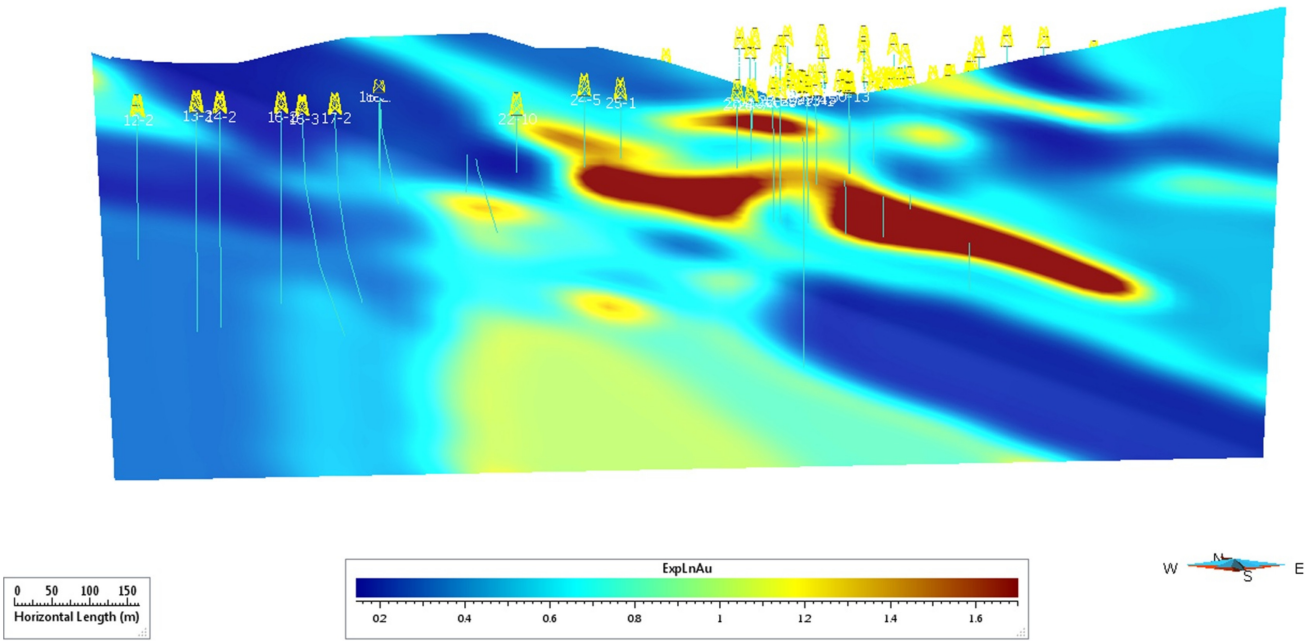

Fig. 8 Ore body No.12 grade DSI map in longitudinal section

vertical continuity of ore body No. 12 at depth and good consistency with C-V results.

2.3 Calculation of Xnp and VH using thresholds from C-V fractal modeling

2.3.1 Calculation of Xnp vertical gradient

We used the thresholds from C-V fractal modeling instead of the levels of thermoelectric coefficients of pyrite in the samples in Eq. (2). The levels f_{I}, f_{II}, f_{IV}, and f_{V} used to calculate the pyrite thermoelectric parameter (Xnp) in Eq. (2) may be unsuitable for the case of the Pujon gold deposit because most of the thermoelectric coefficient data are P-type, and the deep continuation of ore bodies in some parts of the study area is certain by drilling data. Therefore, we attempted to calculate the pyrite thermoelectric parameter (Xnp) using the thresholds from C-V fractal modeling instead of traditional levels in Eq. (2). The continuation of ore bodies at depth was estimated by

the pyrite thermoelectric parameter, and the result was compared with the real lower boundaries of ore bodies confirmed by drilling data.

Data must be measured in more than two levels in order to determine the continuation of ore bodies at depth by the pyrite thermoelectric parameter, and thus we calculated values only for ore bodies of Wondong No. 5, West Kumjomdong No.1, and Kumjomdong Nos. 2, 6, 12, and 14 with more than two levels. The five thresholds determined by C-V fractal modeling are 185, 138, 117, 81, and 45, and thus, six intervals can be created using these five levels. However, only five intervals are necessary to calculate the pyrite thermoelectric parameter. The measured thermoelectric coefficient data were assigned to six intervals and their percentage in each interval was determined. Two intervals were merged into one so that they would reflect variation characteristics of thermoelectric coefficient data in the upper and lower levels, and five intervals were finally prepared for future calculation.

Three threshold groups were used to calculate the Xnp: group 1 [185, 138, 81, 45], group 2 [185, 138, 117, 81], and group 3 [185, 138, 117, 45]. The pyrite thermoelectric

Table 5 Calculated Xnp and continuation of ore bodies at depth in Pujon deposit

Ore bodies	Group	Altitude (m)	Xnp	Continuation (m)	Measured lower level (m)	Calculated lower level (m)	Error (m)
Wondong No. 5	1	1392	8.56	191.03	1190.00	1201.00	−11.00
		1336	−52.94				
	2	1392	−25.23	237.56	1190.00	1154.47	35.53
		1336	−66.67				
	3	1392	−21.62	238.65	1190.00	1153.38	36.62
		1336	−63.73				
West Kumjomdong No. 1	1	1390	72.99	151.41	1250.00	1238.59	11.41
		1352	4.48				
	2	1390	49.64	106.36	1250.00	1283.64	−33.64
		1352	−39.55				
	3	1390	51.10	107.02	1250.00	1282.98	−32.98
		1352	−38.06				
Kumjomdong No. 2	1	1635	90.19	191.53	1550.00	1443.47	106.53
		1591	23.53				
	2	1635	90.19	130.24	1550.00	1504.76	45.24
		1591	−7.84				
	3	1635	94.12	134.69	1550.00	1500.31	49.69
		1591	−1.96				
Kumjomdong No. 6	1	1694	104.35	185.39	1460.00	1508.61	−48.61
		1628	−4.00				
	2	1748	44.00	248.14	1460.00	1499.86	−39.86
		1628	−74.00				
	3	1748	44.00	256.84	1460.00	1491.16	−31.16
		1628	−70.00				
Kumjomdong No. 12	1	1888	63.27	151.83	1750.00	1736.18	13.82
		1873	−127.45				
	2	1888	40.82	133.34	1750.00	1754.66	−4.66
		1873	−135.29				
	3	1888	42.86	125.05	1750.00	1762.95	−12.95
		1873	−133.33				
Kumjomdong No. 14	1	1913	100.00	225.00	1700.00	1688.00	12.00
		1863	33.33				
	2	1902	188.00	208.40	1700.00	1693.60	6.40
		1801	0				
	3	1902	188.00	208.40	1700.00	1693.60	6.40
		1801	0				

parameter and the continuation of ore bodies at depth were calculated using these three groups in Table 5.

To validate the calculations, the lower levels measured by drilling were compared with the levels calculated by Xnp determined using three groups in Table 5. The comparative results show that the calculated lower levels of ore bodies are basically consistent with the measured data by drilling, and the new levels can be used to determine the continuation of ore bodies at depth in the Pujon deposit, although there are some errors and they are different from levels. In Table 5, the negative errors mean that calculated values are greater than the measured ones. Meanwhile, the calculated lower levels by the traditional levels were greatly different from the measured values, and this shows that the traditional levels cannot be used to calculate the Xnp and the continuation of ore bodies at depth in the Pujon gold deposit.

The errors between the measured and calculated values are different from ore bodies in different groups. In group 1, the minimum errors are measured for Wondong No. 5 and West Kumjomdong No. 1. Kumjomdong Nos. 2 and 12 have the minimum errors in group 2, and Kumjomdong No. 6 in group 3. Kumjomdong No. 14 has the minimum errors in groups 2 and 3. It results from the fact that Xnp values are different from levels and ore bodies and the variation in the levels used to calculate the Xnp is different between the upper and lower levels.

2.3.2 Calculation of Xnp vertical gradient

Table 5 gives some of the results with relatively small errors. In real practice, however, we cannot use the levels with minimum errors to calculate the Xnp because the lower levels of ore bodies at depth may be generally unknown.

In this study, we determined which intervals of Xnp vertical gradients resulted in the minimum errors in different levels. To calculate the continuation of ore bodies at depth by Xnp, the Xnp values in the upper levels must be greater than those in the lower levels, and the calculation should be done in all pair levels satisfying the condition. The ore bodies with only two levels such as Wondong No. 5, West Kumjomdong No. 1, and Kumjomdong No. 2 are excluded, so the ore bodies with different levels such as Kumjomdong Nos. 6, 12, and 14 should be selected to calculate the Xnp values in all possible pair levels. If the Xnp vertical gradient is extremely high or low, it will be greatly different from the measured values, and we should select appropriate intervals by considering the continuation characteristics of the ore bodies at depth in the Pujon deposit so that accurate calculations can be achieved and can also be used to calculate the continuation of ore bodies at depth in new areas. It is also important to validate the calculation results in cases with only two levels such as Wondong No. 5, West Kumjomdong No. 1, and Kumjomdong No. 2.

Although Table 5 gives some of the results with relatively small errors in two levels, some ore bodies with different levels such as Kumjomdong Nos. 6, 12, and 14 give different results in all possible pair levels of which Xnp values in the upper and lower levels are satisfied to calculate the continuation of ore bodies at depth. The calculation results in all possible levels of Kumjomdong No. 14 are shown in Table 6. The result in group 3 was the same in group 2. The bold values in Table 6 indicate relatively small errors, and Xnp vertical gradients were 1.33 and 1.56 in group 1 and 1.93, 1.12, and 1.86 in group 2.

As shown in Table 6, the results reveal that the Xnp vertical gradient VH ranges from 1 to 2 when the calculation of continuation at depth results in the minimum errors. The variation characteristics of the Xnp of ore bodies shown in Table 5 is considered and summarized in Table 7. The VH values in Table 7 ranges from 0.74 to 2.35. Although this range cannot be used as an absolute criterion because the error ranges are different from each other, the trend in the range may be an important criterion for calculating the continuation at depth.

The VH values with relatively small errors also range from 1 to 2 in Table 6, indicating that the ore bodies in the Pujon deposit could continue at depth with this kind of variation characteristic in Xnp. Table 7 also shows the VH values with an error of 0. The VH values range from 0.85 to 1.95 for ore bodies except for Kumjomdong No. 2. The VH outlier value of Kumjomdong No. 2 might be the result of possible mistakes in sampling and preparation or measurement errors because of incorrect handling. If the VH values calculated between the upper and lower levels range from 1 to 2 when estimating the continuation of ore bodies at depth by using pyrite thermoelectric properties in the Pujon deposit, then the calculation results could be reliable. Thus, it is concluded that only two levels with VH values ranging from 1 to 2 should be selected to calculate the continuation of ore bodies at depth.

3 Results

In the current study, the method established for the Pujon deposit was applied to estimate the continuation of ore bodies at depth in the Pyongsandok area.

3.1 Characteristics of ore bodies in Pyongsandok

The ore bodies in the Pyongsandok deposit are located at an altitude of 2100 m near the ridge of Puksupaek range, 20 km from Pujon deposit. The country rocks in Pyongsandok are the same as in the Pujon deposit, and they are mainly alaskite

Table 6 Xnp vertical gradient (VH) calculated in different groups of Kumjomdong No.14

Group	Selected altitudes (m)	Xnp intervals	Continuation (m)	Measured lower level (m)	Calculated lower level (m)	Errors (m)	VH (Xnp vertical gradient)
1	1913 ~ 900	100.00 ~ 4.00	40.60	1700.00	1872.40	−172.40	7.38
	1913 ~ 1877	100.00 ~ 9.00	118.50	1700.00	1794.50	−94.50	2.53
	1913 ~ 1863	**100.00 ~ 33.00**	**225.00**	**1700.00**	**1688.00**	**12.00**	**1.33**
	1913 ~ 1856	100.00 ~ 46.00	319.20	1700.00	1593.80	106.20	0.94
	1913 ~ 1801	100.00 ~ 30.00	480.00	1700.00	1433.00	267.00	0.62
	1913 ~ 1775	100.00 ~ 30.00	595.10	1700.00	1317.90	382.10	0.50
	1902 ~ 1900	188.00 ~ 4.00	4.20	1700.00	1897.80	−197.80	92.00
	1902 ~ 1877	188.00 ~ 9.00	54.10	1700.00	1847.90	−147.90	7.16
	1902 ~ 1863	188.00 ~ 33.00	97.80	1700.00	1804.20	−104.20	3.96
	1902 ~ 1856	188.00 ~ 46.00	126.10	1700.00	1775.90	−75.90	3.07
	1902 ~ 1801	**188.00 ~ 30.00**	**248.00**	**1700.00**	**1654.00**	**46.00**	**1.56**
	1902 ~ 1775	188.00 ~ 30.00	312.70	1700.00	1589.30	110.70	1.24
	1863 ~ 1801	33.00 ~ 30.00	4340.00	1700.00	−2477.00	4177.00	0.05
	1863 ~ 1775	33.00 ~ 30.00	7084.00	1700.00	−5221.00	6921.00	0.03
	1856 ~ 1801	46.00 ~ 30.00	825.00	1700.00	1031.00	669.00	0.29
	1856 ~ 1775	46.00 ~ 30.00	1248.00	1700.00	608.00	1092.00	0.19
2	1913 ~ 1900	100.00 ~ −40.00	27.90	1700.00	1885.10	−185.10	10.76
	1913 ~ 1877	100.00 ~ −29.00	83.50	1700.00	1829.50	−129.50	3.59
	1913 ~ 1863	**100.00 ~ 3.00**	**154.70**	**1700.00**	**1758.30**	**−58.30**	**1.93**
	1913 ~ 1856	**100.00 ~ 36.00**	**266.00**	**1700.00**	**1647.00**	**53.00**	**1.12**
	1913 ~ 1801	100.00 ~ 0	336.00	1700.00	1577.00	123.00	0.89
	1913 ~ 1775	100.00 ~ 9.00	453.40	1700.00	1459.60	240.40	0.66
	1902 ~ 1900	188.00 ~ −40.00	3.40	1700.00	1898.60	−198.60	114.00
	1902 ~ 1877	188.00 ~ −29.00	44.60	1700.00	1857.40	−157.40	8.69
	1902 ~ 1863	188.00 ~ 3.00	81.80	1700.00	1820.20	−120.20	4.74
	1902 ~ 1856	188.00 ~ 36.00	117.20	1700.00	1784.80	−84.80	3.31
	1902 ~ 1801	**188.00 ~ 0**	**208.40**	**1700.00**	**1693.60**	**6.40**	**1.86**
	1902 ~ 1775	188.00 ~ 9.00	274.80	1700.00	1627.20	72.80	1.41
	1863 ~ 1801	33.00 ~ 0	4154.00	1700.00	−2291.00	3991.00	0.04
	1856 ~ 1801	46.00 ~ 0	363.00	1700.00	1493.00	207.00	0.64
	1856 ~ 1775	46.00 ~ 9.00	706.70	1700.00	1149.30	550.70	0.33

The bold numbers indicate values with very small errors

of the Ryonhwasan complex. Most ore bodies in Pyongsandok are gently inclined with a SW or NS strike. However, Pyongsan Nos. 9 and 10 exist within steeply inclined fault zones, and they occur as an echelon with a length of 2000 m from west to east and a width of 800 m from south to north. They are divided into three groups: quartz veins, quartz-sulfide, and quartz-silicification zones. Ore bodies can be also divided into gently inclined and steeply inclined. The former intrudes into gray and brown fault zones, and the latter mainly exists in the hanging walls or footwalls of a shungite fault. Pyongsan Nos. 9 and 10 intrude into steeply inclined faults, and they are quartz-silicification zones. The metal ore minerals include pyrites, chalcopyrite, and galena. The nonmetal ore minerals are quartz, K-feldspar, chlorite, and carbonates. The parent rocks around the ore bodies are characterized by silicification, sericitization, chloritization, and K-feldsparthization. Pyongsan No. 9 is located in the east of ore body No. 4 and occurs as fractured and contorted quartz veins.

The strike of the ore body is 160°, with dips varying from 35° to 40° and thickness of 0.6 m, and the average grade is 6.27 g/t with a maximum of 11.83 g/t. There is a brown-colored fault gouge with a width of 0.02–0.03 m in the footwall of the ore bodies where pyrites are oxidized as limonites. The parent rocks in the hanging walls and footwalls of ore bodies are medium- or fine-grained alaskite which have undergone silicification and kaolinization (Fig. 9).

Table 7 Variation characteristics of Xnp of ore bodies in Pujon deposit

Ore bodies	Group	Altitude (m)	Xnp	Error (m)	VH	VH with error of 0
Wondong No. 5	1	1392	8.56	−11.00	1.09	1.03
		1336	−52.94			
	2	1392	−25.23	35.53	0.74	0.87
		1336	−66.67			
	3	1392	−21.62	36.62	0.75	0.88
		1336	−63.73			
West Kumjomdong No. 1	1	1390	72.99	11.41	1.80	1.95
		1352	4.48			
	2	1390	49.64	−33.64	2.35	1.78
		1352	−39.55			
	3	1390	51.10	−32.98	2.35	1.79
		1352	−38.06			
Kumjomdong No. 2	1	1635	90.19	106.53	1.52	3.41
		1591	23.53			
	2	1635	90.19	45.24	2.23	3.41
		1591	−7.84			
	3	1635	94.12	49.69	2.18	3.46
		1591	−1.96			
Kumjomdong No. 6	1	1694	104.35	−48.61	1.64	1.30
		1628	−4.00			
	2	1748	44.00	−39.86	0.98	0.85
		1628	−74.00			
	3	1748	44.00	−31.16	0.95	0.85
		1628	−70.00			
Kumjomdong No. 12	1	1888	63.27	13.82	1.73	1.91
		1873	−127.45			
	2	1888	40.82	−4.66	1.81	1.75
		1873	−135.29			
	3	1888	42.86	−12.95	1.94	1.76
		1873	−133.33			
Kumjomdong No. 14	1	1913	100.00	12.00	1.34	1.41
		1863	33.33			
	2	1902	188.00	6.40	1.94	1.41
		1801	0			
	3	1902	188.00	6.40	1.76	1.92
		1801	0			

It is currently unclear whether Pyongsan No. 9 either cut other gently inclined ore bodies or acted as a path to form them, because drilling has not yet been implemented. The gold in ore minerals in Pyongsan No. 9 is closely related to pyrites, just as the ore bodies in the Pujon deposit. The parent rocks and their alterations in Pyongsan No. 9 are also the same as in the ore bodies of the Pujon deposit. In addition, measurement data for the pyrite thermoelectric coefficients in this area have the same characteristics as the prevailing percentage of P-type and similar intervals in the Pujon deposit. Therefore, it is possible to estimate the continuation of ore bodies at depth by the methodology established using pyrite thermoelectricity in the Pujon deposit.

3.2 Continuation of ore body Pyongsan No. 9 at depth

At this time, borehole No. 518 has already been drilled to study the continuation of ore bodies and reserves at depth, and the altitude of its location was 2180 m. Thermoelectricity measurements were made from the samples from levels at 2150 m and 2100 m to validate the continuation of ore bodies at the location of drilling design. The grains of

Fig. 9 Outcrops and boundaries between ore bodies and parent rocks in Pyongsan No. 9

are smaller than the range of 1 to 2 determined in the Pujon deposit.

To reduce this kind of error, the continuations at depth were estimated in the cases with VH values of 1, 1.5, and 2 (Table 10). The calculated VH values (0.63 and 0.69) were close to 1, and we could select the continuation at depth with a VH value of 1. Its average was 315 m and indicates that Pyongsan No. 9 continues 315 m to 455 m at depth at an altitude of 2150 m.

3.3 Validation

The drilling design predicted the possibility of finding an ore body at an altitude of 1920 m by considering the inclined continuation of the ore body. It was supposed that the ore body would continue at depth with the same strike and dip as

Table 8 Thermoelectricity data and analysis of pyrites from two levels of Pyongsan No.9

No.	Altitude (m)	$\alpha_N/(\mu V \cdot °C^{-1})$			Percent (%)	$\alpha_P/(\mu V \cdot °C^{-1})$			Percent (%)
		Maximum	Minimum	Average		Maximum	Minimum	Average	
1	2150	-	-	-	-	247.30	107.40	167.94	100.00
2	2100	-	-	-	-	234.50	101.00	155.47	100.00

Table 9 Results of continuation calculation

Group	Altitude (m)	f_1	f_2	f_4	f_5	Xnp	Continuation (m)	Erosion (%)	VH
1	2150	32.00	52.00	0	0	116.00	499.30	21.00	0.63
	2100	6.70	70.95	0	0	84.36			
2	2150	32.00	52.00	1.60	0	114.40	455.50	21.40	0.69
	2100	6.70	70.95	4.46	0	79.89			

Table 10 Continuation at depth estimated by VH values

Group	Altitude (m)	Continuation (m)			Lower level (m)		
		1	1.5	2	1	1.5	2
1	2150–2100	316.00	210.67	158.00	1834.00	1939.30	1992.00
2	2150–2100	314.40	209.60	157.20	1835.60	1940.00	1992.80

pyrites from the two levels were prepared for measurements of thermoelectricity, and the results are given in Table 8.

The continuation of ore body Pyongsan No. 9 at depth was estimated by levels determined using C-V fractal modeling in the Pujon deposit (Table 9). As shown in Table 9, the continuation lengths were estimated as 499.3 m in group 1 and 455.5 in group 2. The erosional ratio at an altitude of 2150 m was almost 21%, and the VH values were 0.63 and 0.69, respectively. This indicates that the calculation results may include some errors, because they

on the surface. The calculation results show that the Pyongsan No. 9 would continue 315–455 m at depth to an altitude of 1835–1695 m, meaning that the ore body would be found at an altitude of 1920 m if the current drilling were continued according to the original design.

To validate the prediction results, the drilling continued and the predicted ore body was found at an altitude of about 1920 m. Its thickness was 2.8 m and the gold reserve was 456 kg, with an average grade of 2.57 g/t. The borehole section is shown in Fig. 10. By the calculation, ore body Pyongsan No. 9 extends 85 m to 235 m

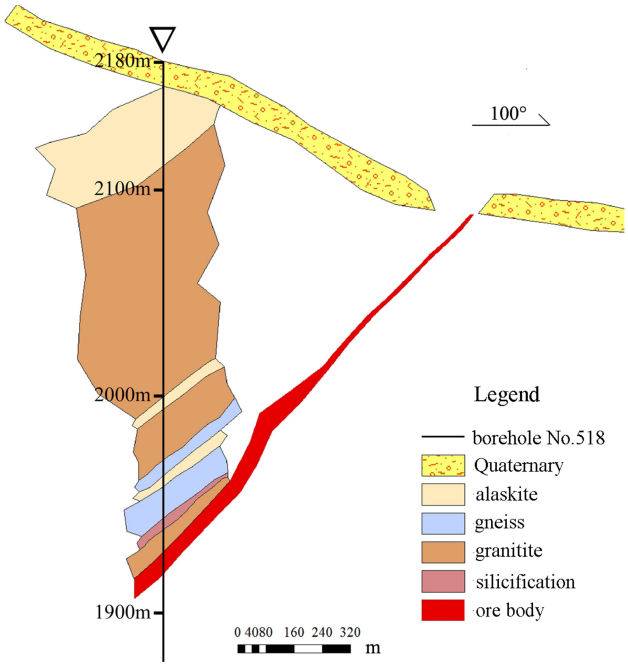

Fig. 10 Longitudinal section map of borehole No. 518

downward from the current borehole location and indicates that the ore body could continue to an altitude of at least 1835 m. The drilling result is consistent with the prediction by the calculation of pyrite thermoelectricity, which shows that the method is feasible for estimating continuation at depth of ore bodies and for the design of future drilling based on the thermoelectric parameter of pyrite calculated by C-V fractal modeling.

4 Discussion

Analysis of the thermoelectric properties of pyrites can provide information about the depth of ore-forming, mineralization degree, and the medium conditions during the formation of deposits, and thus can aid in finding blind ore bodies. The thermoelectric conductive type of pyrite has certain instructive significance to the erosion depth of the ore body. Differences in the thermoelectric properties of pyrite essentially reflect physical and chemical changes during the migration of the ore-forming solution (Geng et al. 2018). According to the vertical zoning sequence of the primary halo in general hydrothermal deposits, halos of Co and Ni often exist in the lower part of the ore body, while those of S and As exist in the upper part. Co and Ni are present as isomorphic substitutes for Fe^{2+}, resulting in N-type conductivity of pyrite. Meanwhile, replacement of S with As and Sb leads to P-type conductivity. In general, the zoning of thermoelectric conductivity in the vertical direction is as follows: upper part of the ore body, P-type; central part, P+N type; and lower part, N-type.

We determined the thermoelectric coefficient values of the pyrite from the Pujon deposit. The thermoelectric conduction type is characterized as P>>N, with some small fluctuations. The percentage of P-type pyrite (P %) is between 93.7% and 100%, and the thermoelectric coefficient of pyrite ranges from 21.04 to 232.19 μV/°C. This indicates the upper part of ore bodies and shows that pyrite formed under conditions of low temperature and sulfur enrichment (Geng et al. 2018). As shown in Fig. 3, the regression line for the average thermoelectric coefficients of the pyrite in levels of the Pujon deposit increase at depth. This is consistent with the thermoelectric theory and indicates that the thermoelectric coefficients of the pyrite can be used to estimate the continuation of ore bodies at depth.

In addition, according to the statistical analysis of the shape of pyrite crystals (Ri and Rim 2001), the percentage of cubic and pentagonal-dodecahedral forms is 49.8% and 36.8%, respectively, in the middle part of the deposit, and 86.29% and 0.29% in the upper part. In the environment of mineral formation, low temperature and pressure, low concentrations of sulfur and iron, and simple components lead to the formation of cubic pyrites due to the slow speed of pyrite crystallization. Meanwhile, relatively high temperature and pressure is suitable for pentagonal-dodecahedral formation. Therefore, in the Pujon deposit, the shape of the pyrite crystals represents the upper and middle part of the deposit and is consistent with the results by thermoelectric coefficient values.

In this work, we calculated the pyrite thermoelectric parameter (Xnp) using the thresholds from C-V fractal modeling instead of traditional levels, and the continuation of ore bodies at depth was estimated by the pyrite thermoelectric parameter, mainly because most of the thermoelectric coefficient data were P-type. The result was compared with the real lower boundaries of ore bodies confirmed by drilling data. Our methodology can be used in other gold camps in the world if pyrite is the chief Au-bearing mineral. However, the levels determined by C-V fractal modeling would be different from one deposit to another. The levels used to calculate the pyrite thermoelectric parameter should be determined by considering the specific conditions of the study area. The application of our methodology would be limited to the deposits where measuring the thermoelectric properties of pyrite is possible throughout the whole deposit. The number of measurement points should be sufficient and their distribution should reflect all levels of the deposit. Thus, our methodology would be useful for estimating the continuation of ore bodies at depth within and around the deposits where mining is in progress.

The VH outlier value of some ore bodies such as Kumjomdong No. 2 might be the result of possible mistakes in sampling and preparation or measurement errors because of incorrect handling. In addition, possible errors can be attributed to Sgrid modeling in GOCAD such as selection of voxel size and fitness criteria of regression segments in C-V fractal modeling. Therefore, it is important to set reasonable parameters in GOCAD modeling and C-V fractal modeling using proper techniques such as trial-and-error to reduce possible errors in our methodology.

5 Conclusions

The Pyongsandok area in the northern part of the Pujon deposit is a relatively less-explored area and is considered to be a promising region in the study area. Thus, the main aim of the current study was to estimate the continuation of ore bodies at depth using the thermoelectric characteristics of gold-bearing pyrite. Specifically, our focus was on answering the question as to how we could estimate the continuation of ore bodies at depth using pyrite thermoelectricity in the Pujon gold deposit where pyrites are dominantly P-type. For this purpose, we created a method including four steps: (1) 3D modeling of ore bodies using surface geological mapping, mining tunnels in different levels, and a borehole dataset; (2) 3D modeling of thermoelectric coefficients from Au-bearing pyrites based on discrete smooth interpolation and concentration-volume fractal techniques; (3) determination of levels used for calculation of the thermoelectric parameter of pyrite by C-V fractal modeling instead of traditional levels; and (4) determination of the thermoelectric parameter vertical gradient of pyrite reflecting the variation characteristics of pyrite thermoelectricity in the Pujon deposit.

The method was first established using data from the Kumjomdong area, a well-explored brownfield, and it was then applied to estimate the continuation of ore bodies at depth in the Pyongsandok area, a less-explored greenfield. The Au grade DSI was applied to validate the results of C-V fractal modeling.

The research results show that (1) pyrites in the Pujon deposit are dominantly P-type, unlike most case studies in this field, and it is not reasonable to use traditional levels to calculate the thermoelectric parameter of pyrite; (2) thresholds determined by C-V fractal modeling can be used as levels to calculate the thermoelectric parameter of pyrite; (3) the thermoelectric parameter vertical gradient of pyrite ranges from 1 to 2 in the Pujon deposit; and (4) ore body Pyongsan No. 9 extends 85 m to 235 m downward from the current borehole location.

Acknowledgements The authors thank the geological survey of Pujon mine for their contributions in providing geological data for the Pujon deposit and their support during the field work. We also appreciate Editor-in-Chief, Chief Editor, Associate Editor, and anonymous reviewers for their thorough reviews of the manuscript and their constructive comments, which helped us to improve this paper.

Author contributions Conceptualization, Kim YH and O CN; methodology, Kim YH and O CN; modeling and validation, Choe KU; measurement and data processing, O CN; original draft preparation, Kim YH; review and editing, O CN; supervision, Hwang KC. All authors have read and agreed to the published version of the manuscript.

Funding There is no funding.

Declarations

Conflict of interest The authors declare no conflict of interest.

References

Abraitis PK, Pattrick RAD, Vaughan DJ (2004) Variations in the compositional, textural and electrical properties of natural pyrite: a review. Int J Miner Process 74(1):41–59. https://doi.org/10.1016/j.minpro.2003.09.002

Afzal P, Fadakar Alghalandis Y, Khakzad A, Moarefvand P, Rashidnejad Omran N (2011) Delineation of mineralization zones in porphyry Cu deposits by fractal concentration-volume modeling. J Geochem Explor 108:220–232

Afzal P, Dadashzadeh Ahari H, Rashidnejad Omran N, Aliyari F (2013) Delineation of gold mineralized zones using concentration-volume fractal model in qolqoleh gold deposit, NW Iran. Ore Geol Rev 55:125–133

Alam M, Li SR, Santosh M, Shah A, Yuan MW, Khan H, Akhte QJA, Zeng YJ (2019) Morphological, thermoelectrical, geochemical and isotopic anatomy of auriferous pyrite from the Bagrote Valley placer deposits, North Pakistan: implications for ore genesis and gold exploration. Ore Geol Rev 112:103008. https://doi.org/10.1016/j.oregeorev.2019.103008

Alam M, Li SR, Santosh M, Zafar T, Hussain Z, Yuan MW, Khan H (2023) Characteristics, provenance, ore genesis and exploration of the Shimshal Valley placer gold deposits in the Karakoram Block, North Pakistan. J Geochem Explor 245:107128. https://doi.org/10.1016/j.gexplo.2022.107128

Bazargani Golshan M, Arian M, Afzal P, Daneshvar Saein L, Aleali M (2025) Application of fractal models for determining the relationship between REEs and faults in North Kochakali coal deposit, Central Iran. Sci Rep 15(1):1276

Chen Z, Chen JP, Tian SF (2018) Application of the content–area (C–A) fractal model and prediction–area (P–A) plot for mineral prospectivity modeling in the Luchun area of Yunnan Province, China. Arab J Geosci 11:206. https://doi.org/10.1007/s12517-018-3515-5

Cheng QM, Agterberg FP, Ballantyne SB (1994) The separation of geochemical anomalies from background by fractal methods. J Geochem Explor 54:109–130

Choe P, Ho D, Yun J, Sin Y, Jo S (2011) Encyclopedia of Korean Geology, Vol. 8, Industrial Publishing House, p 536 (**in Korean**)

Deng H, Zheng Y, Chen J, Yu SY, Xiao KY, Mao XC (2022) Learning 3d mineral prospectivity from 3d geological models using convolutional neural networks: application to a structure-controlled hydrothermal gold deposit. Comput Geosci. https://doi.org/10.1016/j.cageo.2022.105074

Geng HQ, Gu XX, Zhang YM (2018) Characteristics of genetic mineralogy of pyrite and quartz and their indicating significance in the Gaosongshan Gold Deposit, Heilongjiang Province, NE China. Earth Sci Res J 22(4):301–318. https://doi.org/10.15446/esrj.v22n4.57512

Geovia (2015) GEOVIA SurpacTM-Geology and Mine Planning Software. The 3D EXPERIENCE Company, Vancouver. http://www.geovia.com/products/Surpac

Heidari SM, Afzal P, Sadeghi B (2024) Molybdenum and gold distribution variances within Iranian copper porphyry deposits. J Geochem Explor 261:107471. https://doi.org/10.1016/j.gexplo.2024.107471

Hosseini SA, Khah NKF, Kianoush P, Afzal P, Ebrahimabadi A, Shirinabadi R (2023) Integration of fractal modeling and correspondence analysis reconnaissance for geochemically high-potential promising areas, NE Iran. Res Geochem 11:100026. https://doi.org/10.1016/j.ringeo.2023.100026

Karaman M, Kumral M, Yildirim DK, Doner Z, Afzal P, Abdelnasser A (2021) Delineation of the porphyry-skarn mineralized zones (NW Turkey) using concentration-volume fractal model. Geochemistry 81(4):125802. https://doi.org/10.1016/j.chemer.2021.125802

Li S, Zhao G, Santosh M, Liu X, Dai L, Suo Y, Tam PY, Song M, Wang P (2012) Paleoproterozoic structural evolution of the southern segment of the Jiao-Liao-Ji belt, north China craton. Precambr Res 200:59–73

Li RX, Wang GW, Carranza EJM (2016) GeoCube: a 3d mineral resources quantitative prediction and assessment system. Ore Geol Rev 89:161–173

Li CL, Li L, Yuan MW, Alam M, Li SR, Santosh M, Deng CZ, Liu H, Xu GZ (2020) Study on pyrite thermoelectricity, ore-forming fluids and H-O-Rb-Sr isotopes of the Yongxin gold deposit, Central Asian Orogenic Belt: implications for ore genesis and exploration. Ore Geol Rev 121:103568. https://doi.org/10.1016/j.oregeorev.2020.103568

Mallet JL (2002) Geomodeling. Applied Geostatistics Oxford University Press, New York, pp 1–10

Micromine (2015) Micromine Exploration & 3D Mine Design Software. Micromine Pty Ltd., Perth (accessed 25 November 2015). http://www.micromine.com/products-downloads/micromine

Mohammadpour M, Bahroudi A, Abedi M (2021) Three dimensional mineral prospectivity modeling by evidential belief functions, a case study from Kahang porphyry Cu deposit. J African Earth Sci. https://doi.org/10.1016/j.jafrearsci.2020.104098

Paek R, Kang H, Jon G, Kim Y, Kim Y (1993) Geology of Korea, Foreign Languages Books Publishing House, p 619

Paravarzar S, Mokhtari Z, Afzal P, Aliyari F (2023) Application of an approximate geostatistical simulation algorithm to delineate the gold mineralized zones characterized by fractal methodology. J African Earth Sci 200:104865. https://doi.org/10.1016/j.jafrearsci.2023.104865

Pourgholam M, Afzal P, Yasrebi A, Gholinejad M, Wetherelt A (2021) Detection of geochemical anomalies using a fractal-wavelet model in Ipack area, Central Iran. J Geochem Explor 220:106675. https://doi.org/10.1016/j.gexplo.2020.106675

Pourgholam MM, Afzal P, Adib A, Rahbar K, Gholinejad M (2024) Recognition of REEs anomalies using an image fusion fractal-wavelet model in Tarom metallogenic zone, NW Iran. Geochemistry 84(2):126093. https://doi.org/10.1016/j.chemer.2024.126093

Ri C, Rim M (2001) Typomorphic characteristics in types of pyrite crystals in Pujon Deposit. Geol Geogr 47(9):118–129 (**in Korean**)

Sadeghi B (2021) Concentration-concentration fractal modelling: a novel insight for correlation between variables in response to changes in the underlying controlling geological-geochemical processes. Ore Geol Rev 128:103875. https://doi.org/10.1016/j.oregeorev.2020.103875

Shao W, Chen G, Sun D (1990) Method of investigating thermoelectricity of pyrite and its application to pyrites from gold deposits in jiaodong region. Geosci 4:46–57 (**in Chinese**)

Shen J, Li S, Ma G, Liu Y, Yu H (2013) Typomorphic characteristics of pyrite from the linglong gold deposit: its vertical variation and prospecting significance. Earth Sci Front 20:55–75

Ullah J, Li H, Ashraf U, Heping P, Ali M, Ehsan M, Asad M, Anees A, Ren T (2023) Knowledge-based machine learning for mineral classification in a complex tectonic regime of Yingxiu-Beichuan fault zone, Sichuan basin. Geoenergy Sci Eng 229:212077. https://doi.org/10.1016/j.geoen.2023.212077

Wang GW, Pang Z, Boisvert JB, Hao Y, Cao Y, Qu J (2013) Quantitative assessment of mineral resources by combining geostatistics and fractal methods in the Tongshan porphyry Cu deposit (China). J Geochem Explor 134:85–98

Wang GW, Feng Y, Carranza EJM, Li RX, Li ZL, Feng ZK, Zhao XD, Wang DJ, Kong L, Jia WJ, Wen BT (2016) Typomorphic characteristics of pyrite: criteria for 3D exploration targeting in the Xishan gold deposit, China. J Geochem Explor. https://doi.org/10.1016/j.gexplo.2016.01.003

Wang JP, Liu ZJ, Wang KX, Zeng XT, Liu JJ, Zhang FF (2019) Typomorphic characteristics of pyrites from the Shuangwang Gold Deposit, Shaanxi, China: index to deep ore exploration. Minerals. https://doi.org/10.3390/min9060383

Wang Y, Chen JP, Jia DH (2020) Three-dimensional mineral potential mapping for reducing multiplicity and uncertainty: Kaerqueka polymetallic deposit, QingHai province, China. Nat Resour Res 29:365–393

Wang SH, Shen JF, Du BS, Xu KX, Zhang ZS, Liu CY (2021) The relationship between natural pyrite and impurity element semiconductor properties: a case study of vein pyrite from the Zaozigou Gold Deposit in China. Minerals. https://doi.org/10.3390/min11060596

Wang Y, Xiong L, Zhong Z, Ren SL, Zhang G, Wang J, Zhang Y, Song CZ (2022) Typomorphic characteristics of gold-bearing pyrite and its genetic implications for the Fang'an Gold Deposit, the Bengbu Uplift, Eastern China. Minerals. https://doi.org/10.3390/min12101196

Wu JJ, Zeng QD, Wei ZH, Fan HR, Yang KF, Zhang ZM, Li XH, Liang GZ, Xia F (2021) Prospecting potential of the Yanjingou Gold Deposit in the East Kunlun Orogen, NW China: evidence from primary halo geochemistry and in situ pyrite thermoelectricity. Minerals. https://doi.org/10.3390/min11101117

Wu CY, Land XH, Zang H, Wang XH, Zhang P, Deng YL, Lou YM, Jiang K (2024) Typomorphic characteristics and geological significance of pyrite from No. 1 deposit in the Xiongcun district Tiibet. Bullet Mineral Petrol Geochem. https://doi.org/10.3724/j.issn.1007-2802.20240015

Xiao K, Li N, Porwal A, Holden E, Bagas L, Lu Y (2015) GIS-based 3D prospectivity mapping: a case study of Jiama copper-polymetallic deposit in Tibet, China. Ore Geol Rev 71:357–367

Xue J, Li S, Sun W, Zhang Y, Zhang X (2014) Characteristics of the genetic mineralogy of pyrite and its significance for prospecting in the Denggezhuang gold deposit, Jiaodong peninsula, China. Sci China Earth Sci 57(4):644–661

Yang G, Zhang YH (1991) The relationship between pyrite thermoelectricity and ore forming temperature and its significance in gold deposits. Geol Inf Shandong 1:20–25 (**in Chinese**)

Yilmaz H, Sadeghi B, Cohen D (2022) The efficiency of fractal techniques in geochemical anomaly delineation within BLEG and <180 ppm stream sediments in Western Turkey. J Geochem Explor 236:106957. https://doi.org/10.1016/j.gexplo.2022.106957

Yousefi M, Carranza EJM (2015) Prediction–area (P–A) plot and C-A fractal analysis to classify and evaluate evidential maps for mineral prospectivity modeling. Comput Geosci 79:69–81

Zhang ZQ, Wang GW, Ding YN, Carranza EJM (2021) 3d mineral exploration targeting with multi-dimensional geoscience datasets, Tongling Cu(-Au) district, China. J Geochem Explor 221:106702. https://doi.org/10.1016/j.gexplo.2020.106702

Zuo RG, Wang J (2015) Fractal/multifractal modeling of geochemical data: a review. J Geochem Explor. https://doi.org/10.1016/j.gexplo.2015.04.010